Advanced Steel Construction – Vol. 21 No. 3 (2025) 253–264
DOI:10.18057/IJASC.2025.21.3.7

STUDY ON FRACTURE BEHAVIOR OF CHS-X JOINTS WITH WELD DEFECTS

Jia-Xing Wang [1], Xiao-Gui Shi [1], Zheng-Lei Liu [1], Ting Ding [1], Qiu-Zhan Xiang [2] and Zheng-Hua Huang [1, *]

[1] *School of Civil Engineering, Guizhou University, Guiyang550025, China*

[2] *Experimental Center of the School of Civil Engineering, Guizhou University*

* *(Corresponding author: E-mail: zhhuang@gzu.edu.cn)*

A B S T R A C T

To study the fracture behavior of circular hollow section (CHS) X-joints with weld defects, an axial tensile static load test was performed on one penetration welding specimen and two non-penetration welding specimens. The VUSDFLD subroutine in the ABAQUS software is utilized to perform finite element analysis (FEA) of CHS-X joints with weld defects. The simulation is based on micromechanical fracture models (VGM model and SWDM model). The results demonstrate that both VGM and SWDM models can precisely forecast the fracture of CHS-X joints, regardless of the presence or absence of weld defects. The accuracy of the simplified weld defects model using the equivalent width method and equivalent area approach is confirmed by comparing it with the test findings. In the comparison of fracture displacement and ultimate load error between FEA and testing, it was shown that the error of the VGM model is within 21%, and the error of the SWDM model is within 17%. The numerical simulation of the SWDM model is closer to the test results than that of the VGM model, which can be well applied to the fracture prediction and fracture path simulation of CHS-X joint defective weld. This paper provides a new method and perspective for analyzing and evaluating the weld fracture behavior of CHS-X joints with weld defects, serving as an important reference for predicting the bearing capacity of CHS-X joints with non-penetration welding in actual engineering applications.

A R T I C L E   H I S T O R Y

Received: 12 November 2024
Revised: 3 January 2025
Accepted: 8 January 2025

K E Y W O R D S

CHS-X joints;
Defective weld;
Fracture behavior;
Micromechanical fracture models;
Ultimate bearing capacity

1. Introduction

The possible defects in the welding process of the CHS-X joints seriously affect the quality and performance of the joints. In engineering practice, welding is a common method of metal connection for joining two or more metal parts together. Research has demonstrated that the quality of welding has a direct impact on both the quality and lifespan of the workpiece [1–4]. The presence of welding defects in the CHS-X joints will have a detrimental impact on the strength and stability of the welded components, perhaps resulting in their failure. Thus, it is crucial to possess thorough comprehension and efficient measures to prevent these weld defects. Insufficient tool current or excessive gun movement speed during welding might lead to incomplete penetration weld defects. Incomplete penetration defects are a type of weld defect that occurs when there is insufficient fusing of the weld metal, leading to an incomplete fusion area at the root of the welding section [5–7]. Hence, it is of great significance to comprehensively detect and analyze the welding defects of CHS-X joints to improve the overall welding quality.

Traditional fracture mechanics methods, including stress intensity factor, crack tip opening displacement (CTOD), and J-integral approach, have been extensively employed in the investigation of fracture issues in steel structures throughout the last few decades [8–10]. Currently, the predominant micromechanical fracture model used for predicting monotonic tensile fracture is the Void Growth Model (VGM) established by Rice et al. [11]. This model characterizes the stress state of materials by examining changes in stress triaxiality. The accuracy of the VGM model criterion is verified through a sequence of tests and FEA [12–18]. Yin et al. [19] performed monotonic tensile fracture tests on specimens with single-sided U-shaped and V-shaped notches. The VGM model and VGM-based continuous damage criterion were employed to simulate the ductile fracture of these specimens. The FEA accurately predicted the load-displacement curve, which was confirmed by the test data, thus validating the correctness of both fracture criteria. Kanvinde et al. [20] proposed a Cyclic Void Growth Model (CVGM) by studying the positive and negative changes of triaxial stress under cyclic loading. Han et al. [21] studied the influence of hysteresis characteristics of circular hollow section (CHS) X joints on the seismic performance of steel pipe structures by using the CVGM model. Through experiment and FEA, the hysteresis curve and crack propagation of the joints under cyclic load are evaluated. The results show that the experiment and FEA results are highly consistent, and the error of crack load is 10.8% and 5.7%. Recent research in fracture mechanics has demonstrated that, apart from stress triaxiality, the Lord's angle parameter is also a significant determinant of the plastic flow and toughness failure of metallic materials. Smith et al. [22] introduced the Lord's angle parameter based on the CVGM model and proposed the Stress Weighted Damage Model (SWDM). He et al. [23] designed five monotonic tensile specimens under different stress states, extracted the stress triaxiality, Lord's angle parameters, and equivalent plastic strain at the initial fracture point of each specimen, and calibrated the unknown parameters of the VGM model and SWDM model for Q355B steel base metal and weld metal.

While the study of micromechanical fracture models has reached a high level of development, research on steel structures with defects is limited. Steel structures are prone to various defects, which will affect their safety performance [24-28]. Aranđelović et al. [29] fabricated different combinations of defects and performed tests and numerical simulations. They found that the welded joints with misalignment and insufficient root penetration were the weakest and could be affected by internal defects. Zhu et al. [30] analyzed the effects of circumferential weld defects on the fracture behavior of X80 pipes under internal pressure and bending forces using ABAQUS. The findings indicate that the impact of defect depth on performance is more substantial than that of defect perimeter. Geng et al. [4] studied the linear elasticity of welded thin-walled steel tubes with circular arc weld defects under bending loads, modelling these defects as circular arc cracks. They calculated the energy release rate (J-integral) using finite element methods and found that the arc length influences the stress intensity factor. Mazurkiewicz et al. [31] examined how multiple defects—such as misalignments, undercuts, incomplete root penetration, and excess weld metal—affect the performance of welded joints, revealing that stress concentration from different defects significantly impacts yield stress and plasticity, especially in misaligned joints. Lai et al. [32] investigated butt fusion-welded MDPE tube joints with varying sizes of spherical and planar defects, addressing inadequate adhesion during welding in their tests and simulations. Research indicates that defects measuring 15% of the tube wall thickness do not affect pipeline strength. However, as defect sizes increase to 30% and 45% of the wall thickness, failure strain decreases significantly. Wang et al. [33] found that incomplete penetration weld defects reduce both the average tensile and impact strength in 316L welded joints. Yan et al. [34] showed that high-temperature defects in the weld zone cause stress concentration and decrease yield strength, leading to brittle fractures. Arandjelovic et al. [35] found that secondary defects combined with vertical misalignment are most likely to cause welding failures. Most studies on welding defects focus on their impact on mechanical properties, with little research on fracture behavior. Liao et al. [36] used J-integral, VGM, and SMCS models to predict fractures in Q460C beam-column joints with initial defects, while Xing et al. [37] assessed Q235 steel corrosion, finding a ductility reduction of about 36.811%, with SWDM and LOU models outperforming VGM in fracture predictions. While Liao and Xing studied initial defects and corrosion, they did not address fractures in CHS-X joints with weld non-penetration defects. Given the prevalence of incomplete penetration during welding and its tendency to cause cracks during cooling, further investigation into the fracture performance of CHS-X joints with incomplete weld penetration is necessary.

To study the fracture properties of CHS-X joints with initial defects, three joints were designed: one with a penetration weld and two with incomplete penetration welds, all for axial loading tests. All joints were made from Q355B steel. The simulation of these joints utilized the Void Growth Model (VGM) and Stress Weighted Damage Model (SWDM) within the VUSDFLD subroutine of ABAQUS software using Fortran. The study evaluated the accuracy of both models in predicting fractures by comparing simulation results with actual test specimens. This research provides valuable insights for the safety analysis of CHS-X joints with weld defects.

2. Micromechanical fracture model

2.1. VGM model

Rice [11] et al. pointed out that the cavity expansion rate is exponential with the triaxiality of the stress state and finally derived the VGM criterion, which is expressed as:

$$\eta = \frac{\ln\left(\frac{R}{R_0}\right)}{C} = \int \mathrm{e}^{AT} \mathrm{d}\bar{\varepsilon}_{\mathrm{p}} \tag{1}$$

where η is a material property constant, R is the instantaneous hole diameter, T is stress triaxiality, $T = \sigma_{\mathrm{m}}/\sigma_{\mathrm{e}}$, σ_m is average stress, σ_{e} is equivalent stress, C and A are parameters to be fitted, $d\bar{\varepsilon}_p$ is the equivalent plastic strain increment. Equation (1) can be expressed by the following damage variable:

$$D = \int Ce^{AT} d\bar{\varepsilon}_p \tag{2}$$

When damage variable D=1, the material can be considered to break.

2.2. SWDM model

Smith et al. [22], based on the CVGM model, considered the damage accumulation problem of members under low-stress triaxial degree, introduced the Lode angle parameter to describe the partial stress state, and used the hyperbolic sine function to replace the exponential function to adjust the fracture model, and proposed SWDM model, which is expressed as:

$$D = e^{\lambda\varepsilon_{\mathrm{p}}} \int_0^{\varepsilon_{\mathrm{p}}} C(\beta e^{A^{+}T} - e^{-A^{-}T}) e^{\kappa\xi} d\varepsilon_{\mathrm{p}} \tag{3}$$

$$\xi = cos\ (3\theta) = \frac{3\sqrt{3}J_3}{2J_2^{3/2}} \tag{4}$$

where λ represents the cyclic degradation rate, while β denotes the relative rate of damage, with its value fixed at 1.0. The material parameters, A^+, A^-, and κ, can be determined through test calibration. The lode angle parameter ξ varies within the range of –1 to 1, where ξ=1 signifies the axisymmetric tensile state, and ξ=0 corresponds to the plane strain state. θ is the Lode angle, and J_2 and J_3 represent the second and third invariants of the deviator stress tensor, respectively.

Rewrite Eq. (3) into incremental form, and express SWDM fracture model in the form as:

$$dD = e^{\lambda\varepsilon_{\mathrm{p}}} \cdot C \cdot (e^{A^{+}T} - e^{-A^{-}T}) e^{\kappa\xi} d\varepsilon_{\mathrm{p}} \tag{5}$$

Eq. (5) is simplified to the monotonic load form of the SWDM model, as presented in Eq. (6).

$$D = \int Ce^{AT} e^{k\xi} d\bar{\varepsilon}_p \tag{6}$$

When D=1, the material can be considered to start to break.

Reference [23] predicted the fracture behavior of both the base metal test piece and the weld metal using two models. The results showed that the VGM model is primarily applicable to test pieces under high-stress triaxial states and is not applicable to test pieces under low-stress triaxial states or shear states with complex stress distributions. In contrast, the SWDM model, which considers the effect of the Lord's angle parameter, can accurately simulate the damage extent of the joint under various stress triaxial states.

Under monotonic loading, a material point in an element reaches the critical ductile fracture state when it satisfies Eq. (2) and (6), initiating fracture. Notably, the joints maintain their bearing capacity even after cracking. Thus, post-cracking, a detailed analysis of the joint's mechanical properties is crucial for assessing its limit state. To replicate crack evolution, we undertake secondary development of the finite element (FE) software by integrating the VGM and SWDM models into the VUSDFLD subroutine using Fortran and embedding them in the ABAQUS interface. This setup allows the simulation of crack initiation and propagation within the joints.

The VUSDFLD subroutine mainly defines the state variables, and the state variables of the unit material points need to be updated during each calculation and analysis. In order to realize the crack propagation behavior of the joints after cracking, the method of birth and death element is adopted. When the state variables of the element material point meet the micromechanical fracture criterion, they will be deleted from the whole model and no longer participate in the subsequent calculation. The method of birth and death element first needs to define the deleted state variables in the VUSDFLD subroutine. It needs to be set in the property column of ABAQUS software before the formal analysis. Typically, a value of 1 for the deletion state variable indicates that the unit material point is active and actively participates in the model calculation. Conversely, a value of 0 for the deletion state variable signifies that the unit material point is in a failed state and does not contribute to the model calculation.

3. CHS-X joints fracture test

3.1. Design of joints specimens

Design three CHS-X joints, where specimen GX-1 is fillet weld without weld defects, specimen GX-2 is fillet weld with weld defects, and specimen GX-3 is butt weld with weld defects. The chord and brace of these joints consist of cylindrical steel tubes, and the steel tubes of specimens are Q355B steel tubes. Refer to Table 1 for the dimensions and geometric parameters of these test joints, and consult Fig. 1 for the geometric dimensions.

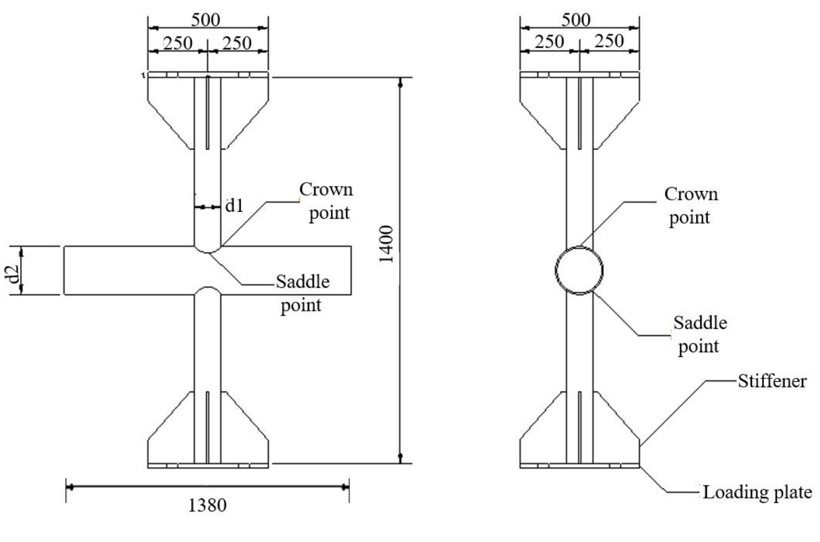

Fig. 1 Geometric dimension of specimen GX-1(unit: *mm*)

Table 1
Dimension and geometrical parameters of test joints

Specimen	Chord *d2×t1*	Brace *d1×t1*	h_f (*mm*)	β	γ	Weld form	Weld defects
GX-1	180×6	121×5	9	0.67	15	Fillet weld	No
GX-2	219×7	121×6	9	0.55	15.64	Fillet weld	Yes
GX-3	245×8	121×7	9	0.49	15.31	Butt weld	Yes

Where β is the ratio of brace diameter to chord diameter, γ is the chord radius-to-thickness ratio, and h_f is the weld size.

3.2. Material characteristics

As shown in Fig. 2, the micromechanical fracture parameters and true stress-plastic strain of Q355B steel calibrated by reference [22] are adopted. The elastic modulus of steel tube base material is 210392 MPa, yield strength is 355.49 MPa, the elastic modulus of weld metal is 206651.71 MPa, yield strength is 384.44 MPa, and Poisson's ratio is taken as 0.3. The fracture parameters of the VGM model and SWDM model are shown in Table 2 and Table 3.

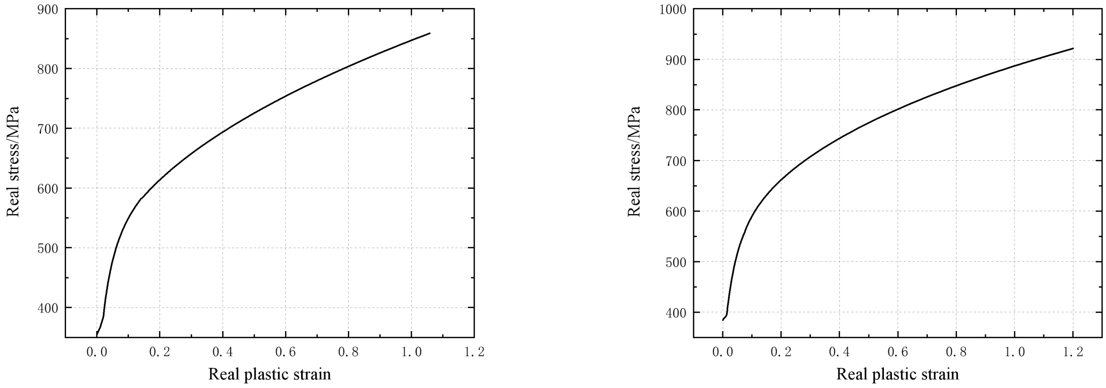

(a) base metal (b) weld metal

Fig. 2 Real stress- plastic strain curves

Table 2
Parameters of VGM model

Material	*C*	*A*	*K*
Base metal	0.466	1.232	--
Weld metal	0.255	1.537	--

Table 3
Parameters of SWDM model

Material	*C*	*A*	*K*
Base metal	0.844	0.635	0.081
Weld metal	0.802	0.771	-0.381

3.3. Loading mode

This test is carried out with the designed triangular reaction frame. The triangular reaction frame is securely fastened to the laboratory floor using ground anchor bolts. The brace of the test joint specimen is securely fastened to the triangle reaction frame at one end using bolts, while the other end is bolted to the MTS servo actuator. The actuator is attached to the laboratory reaction wall. The two ends of the chord are free and placed vertically. Fig.3 displays the test loading equipment.

The unidirectional axial tensile load is applied to the right brace, and displacement control is used. To ensure the smooth development of deformation and stress in the joints, as well as to monitor and obtain the real-time response of the structure under various load levels, the strain rate should be less than 0.00007 s^{-1}, the loading rate is set at 0.75 *mm/min*, according to the strain rate requirements specified in the Chinese and European tensile test specifications for metallic materials [38-39]. The test process is divided into two stages: preloading and formal loading. The purpose of preloading is to verify that the testing instrument can perform normally. During the formal loading stage, a loading speed of 0.75 *mm/min* is used to observe the deformation of the joint specimens and the process of crack propagation as the joints sustain damage. The load-displacement curve is monitored in real-time, with particular attention to the peak point of the curve until joint failure occurs.

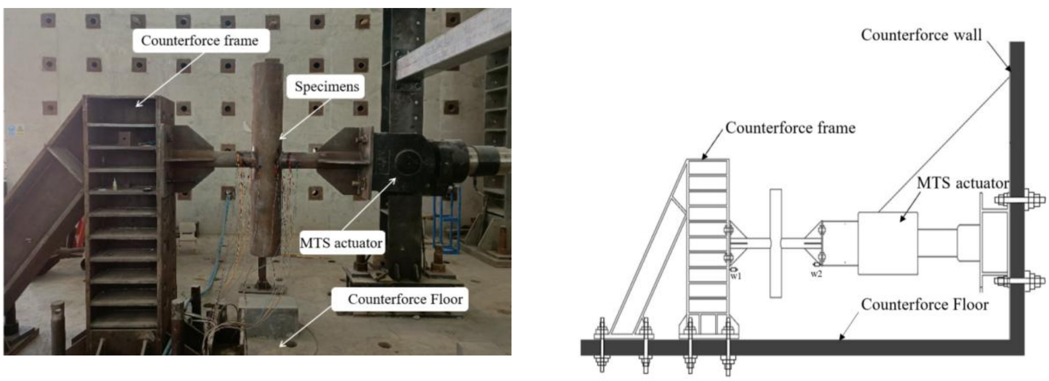

(a) Test field (b) Diagram of test loading device

Fig. 3 Test loading device

3.4. Test process and failure phenomenon of joints

Fig. 4 illustrates the fracture condition of specimen GX-1. A crack was observed at the saddle point of the weld where the brace and the chord intersected on the right side of the front side of the test piece. As the load increases, the crack propagates from the saddle point of the weld to the crown point on both sides. The crack propagation process is shown in Fig. 4. The gradual increase of load leads to large dent deformation of the chord wall and gradual flattening of the chord. At the same time, the crack on the right side of the brace in front of the joint also spreads from the saddle point to the crown point, the crack length gradually increases, and the crack width gradually increases along the axial direction of the brace. When the load reaches 421 *kN*, there is obvious dent deformation of the chord, the crack on the weld expands to the crown point, the crack width is significantly increased, and the joint loses the ability to continue bearing, that is, the maximum bearing capacity is reached, and the joint is damaged, which belongs to the weld failure form [32]. The destruction of the joint test piece is shown in Fig. 5.

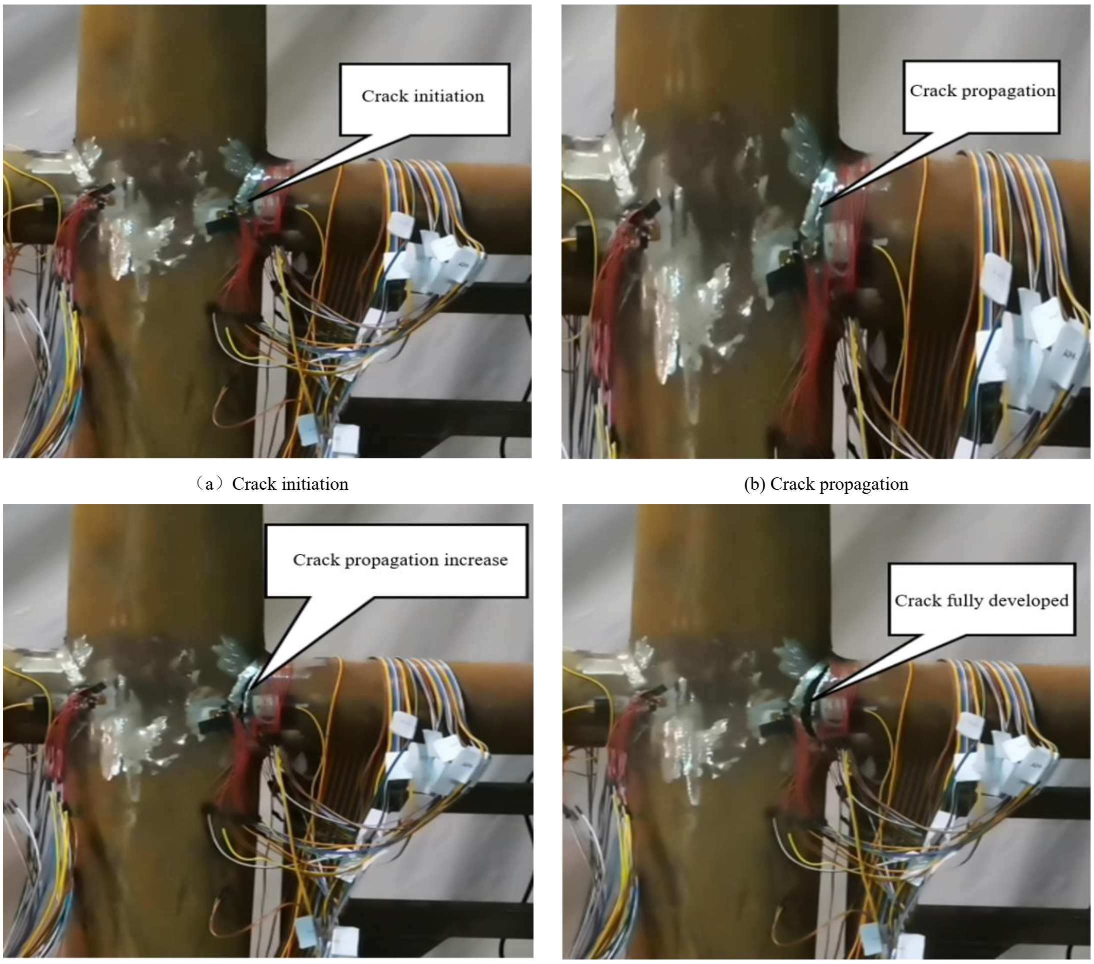

（a）Crack initiation (b) Crack propagation

(c) Crack propagation increase (d) Crack fully developed

Fig. 4 GX-1 Crack propagation process

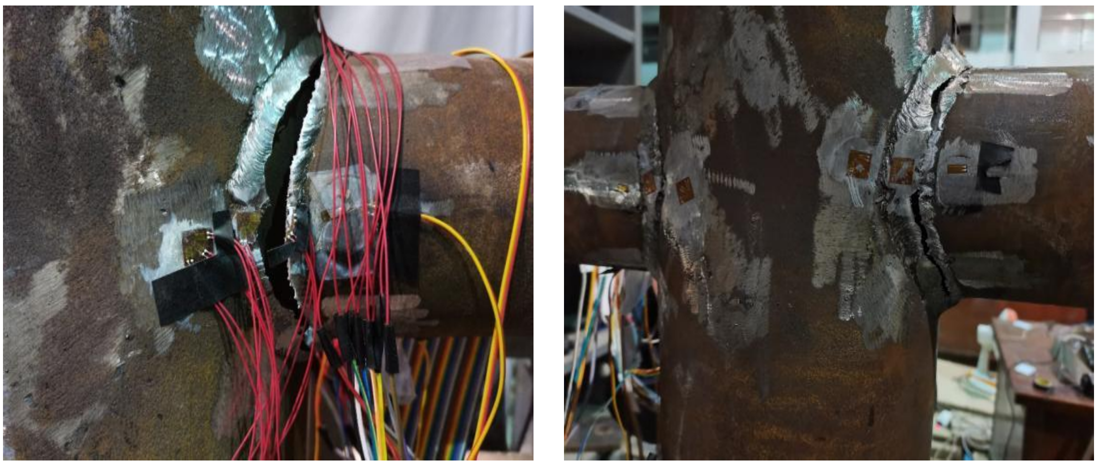

Fig. 5 Failure mode of joint specimen GX-1

Fig. 6 illustrates that as the load increases, specimen GX-2 has large dent deformation, resulting in the eventual flattening of the chord. At the moment the load hits 383.04 *kN*, an abrupt and distinct sound will be audible, indicating the sudden separation of the chord and brace. At this time, the brace of the joint is separated from the weld, and it is difficult to capture the picture of the weld crack from appearing to fracture during the failure process. Fig. 6 shows the final failure form of the joint, in which the failure mode is weld penetration zone fracture and incomplete penetration zone separation.

For joint specimen GX-3, no significant flattening of the chord occurred as the load applied to both ends of the specimen increased. When the load is loaded to 334.72 *kN*, a crisp sound is heard, the bearing capacity drops sharply, and the specimen is damaged. At the saddle of the weld in front of the specimen, the brace is separated from the weld, and there is no fracture crack at the weld behind the specimen. The failure mode of the weld joint of specimen GX-3 is fracture of the weld penetration zone, separation of the non-penetration zone, and short failure time. It is difficult to accurately record the crack growth in the process of weld crack from appearance to failure, and the final failure form of the joint is shown in Fig. 7.

(a) Damage pattern in front of the joint (b) Damage form behind the joint (c) The chord deformation morphology

Fig. 6 Failure mode of joint specimen GX-2

(a) Damage pattern in front of the joint (b) Damage form behind the joint (c) The chord deformation morphology

Fig. 7 Failure mode of joint specimen GX-3

3.5. Test results discussion

Due to the complete penetration of the weld seams in specimen GX-1, stress concentration was high at the joint saddle during the tensile process. Therefore, the cracking point first appeared at the joint saddle, and then the weld crack propagated along the intersecting line, ultimately causing the specimen to lose its bearing capacity and fail. In contrast, although specimen GX-2 has defective welds, its load-displacement curve show a plastic stage, and the chord undergoes significant deformation, with an ultimate bearing capacity of 383.04 *kN*. The time from cracking to fracture in the saddle weld of specimen GX-2 joint is short. Although the deformation of the chord can serve as a precursor to fracture, sudden fracture still poses a potential danger to the engineering structure. The reason for the failure of specimen GX-2 is that there is a small area of incomplete fusion between the weld and the brace. As for specimen GX-3, due to the small penetration area of the weld and the large non-penetration area, the weld defects were significant. The load-displacement curve did not show obvious plastic deformation, and the chord did not undergo dent deformation after fracture. Specimen GX-3 fractured at a load of 337.42 *kN*, with a rapid failure time and no signs of pre-fracture.

Fig.8 displays the load-displacement curves for the three specimens. From the load-displacement curve of specimen GX-2, it can be seen that it shows a plastic phase, while specimen GX-3 does not exhibit obvious plastic deformation. Observing the deformation of the chord, it is evident that the chord of specimen GX-3 undergoes no significant deformation. Regarding the form of fracture, the time from cracking to joint fracture in the weld of both specimens is very short, indicating sudden fracture. However, specimen GX-2 has a larger weld penetration area, and its chord exhibits concave deformation, which can serve as a precursor to joint fracture. In contrast, the joint fracture of specimen GX-3 is sudden, with no precursors before fracture. These differences are primarily attributed to the larger weld penetration area in GX-2 compared to the smaller area in GX-3, and they are quite similar to those observed by Lai [32], who studied butt fusion welded MDPE pipe joints with spherical and planar defects of various sizes through tensile tests and finite element analysis. That is, when the weld penetration area is large, the joint strength decreases slightly, whereas when the weld penetration area is small, the joint strength decreases significantly. In order to enhance the performance of joints and prevent similar issues, it is imperative to study CHS-X joints with weld defects, verify that the design satisfies the load-bearing criteria, and carry out comprehensive quality inspection and monitoring to guarantee the safety and stability of the structure.

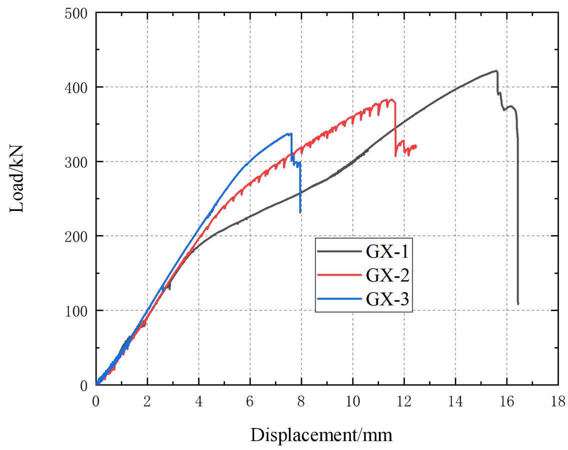

Fig. 8 Load-displacement curve of test specimens

4. Simplification of weld defects and finite element modelling

4.1. Weld defects analysis

The weld defects of specimen GX-2 are shown in Fig. 9, and the brace breaks at three positions, which indicates that the three welds are fused with the brace. The first weld penetration zone fracture occurs at the crown point, and the fracture point size is 36.8 *mm* long and 8.6 *mm* wide. The second weld penetration zone fracture occurs at the saddle point, and the fracture point size is 12.2 *mm* long and 4 *mm* wide. The third weld penetration zone fracture point is located at the crown on the other side, and the fracture point size is 19.4 *mm* long and 4 *mm* wide. Other weld penetration areas are the bright areas shown by the red curves in the figure. The weld penetration widths of these areas vary. The average width of the weld penetration area on the front side of the joint is 5.2 *mm*, while the average width of the weld penetration area on the behind side of the joint is 5.24 *mm*. In addition, the front of the joint has an 18 *mm* long weld penetration area at the saddle point.

(a) Brace and weld penetration breakpoints (b) Weld defects in the front side of joint (c) Weld defects in the behind side of joint

Fig. 9 Weld defects distribution of specimen GX-2

Fig. 10 Simplified weld defects finite element modelling of specimen GX-2

(a) Weld defects in the front side of joint (b) Weld defects in the behind side of joint (c) Simplification of weld defects

Fig. 11 Incomplete penetration weld zone of GX-3 and simplified finite element model

The weld defects of specimen GX-3 are shown in Fig. 11. The failure form is the separation between the weld and brace at the saddle point. The red curve light area in the figure is the part of weld and brace penetration. There was an area of about 23 *mm* in length at the saddle of the brace without any traces of light or fracture, suggesting that this part of the weld was not fully fused with the brace. There is no fracture crack on the rear weld of specimen GX-3, indicating that the rear weld of specimen GX-3 is fused with the brace. Therefore, during finite element modelling, only the defects of welds on the front side of the specimen are considered.

4.2. FEA and welds simplification

The FEA software [40] ABAQUS was used to create solid element models of the chords, braces, and welds. The test piece GX-1 is modeled by directly merging the weld, parent tube, and brace. The element type selected is C3D8R. 0.5 *mm* is taken as the root clearance between the chord and brace. In order to meet the requirement of feature-length L^*, local refinement is applied to the joints weld and its surroundings. The grid size is set at 0.3 *mm* away from the weld-seam area, and the grid size gradually increases to 6 *mm*. The joint constraint condition and load action mode are that the chord end is free, the symmetric axial monotonic load is applied to the section of the brace end, and the symmetric constraint condition is applied to the symmetric surface. Figs. 12 and 13 show the finite element modelling of fillet and butt welds, while the saddle and crown points of the weld model are illustrated in Figs. 14 and 15. The finite element model of the test specimens is shown in Fig. 16.

Due to the highly irregular welding defect areas in specimens GX-2 and GX-3, which include variations in weld penetration size and incomplete penetration areas, creating an accurate finite element model that simulates the actual shape of weld defects is very complex and difficult to realize. Drawing on the simplified methods for assessing weld defects found in the literature [41-44], this study proposes the equivalent width method and the equivalent area method. These approaches overlook the geometric characteristics of weld defects, focusing instead on the impact of their location and area on the specimens. The primary goal is to simplify the analysis of weld defects, reduce model complexity, and facilitate the construction of finite element models for analysis and calculations. Both methods operate under the assumption that the stress concentrations arising from the actual shape and the equivalent shape of a defect have an equal effect on the ultimate bearing capacity at fracture. However, this assumption overlooks variations in fracture-bearing capacity due to shape differences, which may potentially lead to certain errors. These discrepancies will be explored in relation to both test and FEA results. When employing the equivalent width and equivalent area methods, the shape of the weld defect is simplified to a regular form without detailed consideration of its specific geometric characteristics. For example, as illustrated in Fig. 10, the test specimen GX-2 depicts the weld defects simplified as weld seams with a width of 5.22 mm at the bottom of the brace, both in front of and behind the joint. In this region, these weld seams are entirely fused with the brace. During finite element modelling, the braces of the penetration part shall be bound with the welds, and the parts without penetration shall not be subject to any constraint treatment.

For specimen GX-3, a 23 *mm* long weld at the saddle is not penetrated. During modelling, this weld and brace at the corresponding position should not be subjected to any constraint treatment. The total length of the front weld fracture area of specimen GX-3 is 170.5 *mm*, and the sum of the areas of the front penetration areas is calculated to be 347.82 mm^2. The weld width of the weld penetration area is calculated to be 2.04 *mm* based on the area equivalent principle. As shown in Fig. 11, in the finite element modelling, the weld joint with a front length of 170.5 *mm* and a width of 2.04 *mm* is considered to be connected to the brace. The rest of the front weld of the joint is not subject to any constraint, and all welds at the back of the joint are fully penetrated and connected with the brace.

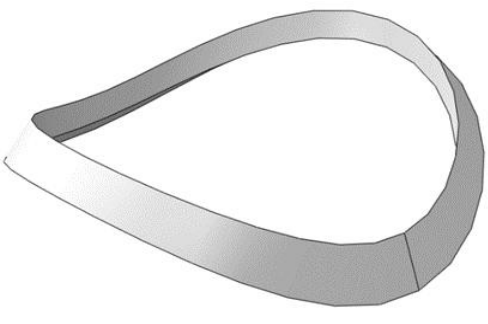

Fig. 12 Three-dimensional diagram of fillet weld

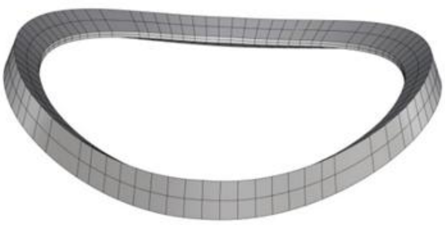

Fig. 13 Three-dimensional diagram of butt weld

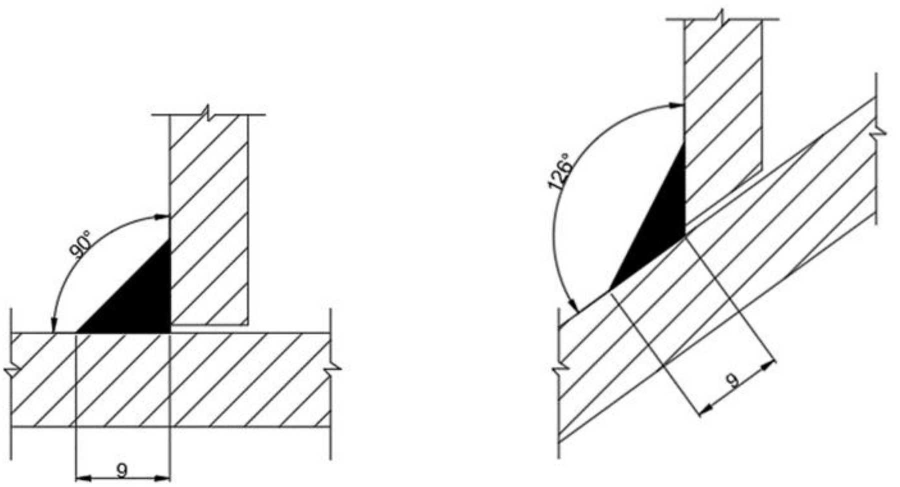

（a）Fillet weld at crown point

（b）Fillet weld at saddle point

Fig. 14 Geometric dimension of fillet weld

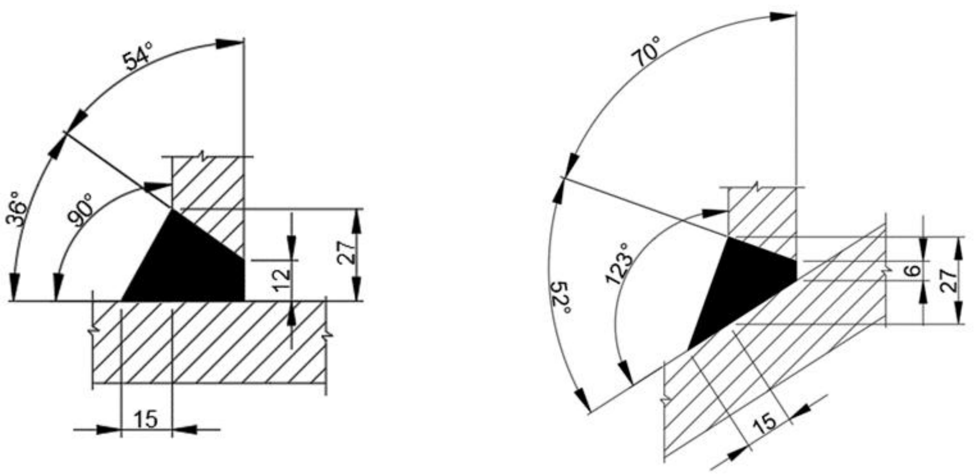

（a）Butt weld at crown point

（b）Butt weld at saddle point

Fig. 15 Geometric dimension of Butt solid welds

(a) GX-1 (b) GX-2 and GX-3

Fig. 16 FE model of specimens

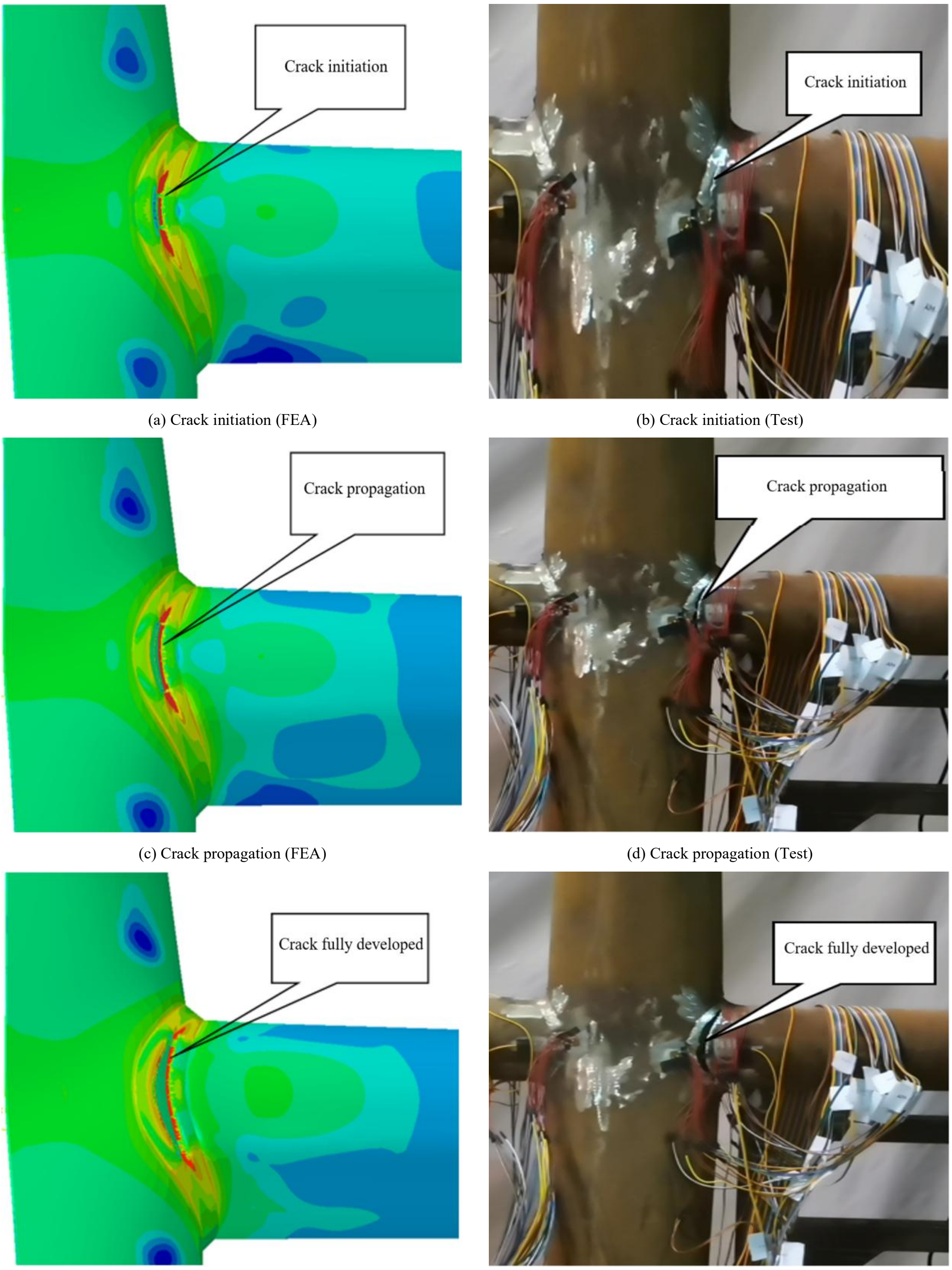

(a) Crack initiation (FEA) (b) Crack initiation (Test)

(c) Crack propagation (FEA) (d) Crack propagation (Test)

(e) Crack fully developed (FEA) (f) Crack fully developed (Test)

Fig. 17 Crack propagation comparison of GX-1

4.3. Comparison between numerical simulation results and test results

Based on the analysis of the crack point in the specimen GX-1 model, it is observed in Fig. 17 that the crack propagation path of the FEA results is consistent with the test results, and the failure of the joint is the failure of the weld. Since the stress concentration at the joint saddle point is relatively serious, the weld crack occurs at the joint saddle point. As the load continues to increase, cracks will propagate from the saddle point along the intersection line of the CHS-X joint to the crown point, and the length and width of the cracks will gradually increase, ultimately leading to fracture and failure of the joint and loss of bearing capacity. The crack propagation process and ultimate bearing capacity of the CHS-X joint, as predicted by the VGM and SWDM models, show a strong agreement with the test data. This finding aligns with the conclusion stated in reference [45], demonstrating the accuracy of FEA.

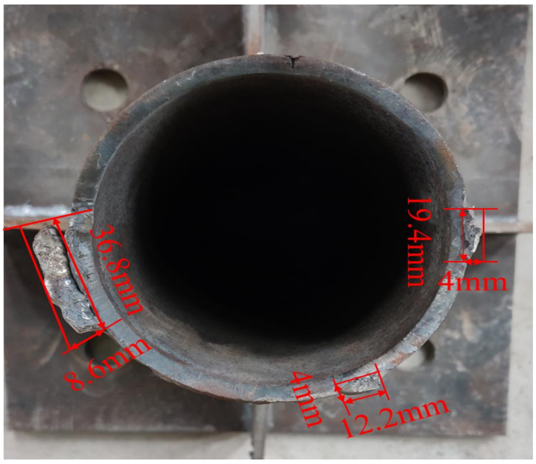

(a) Fracture point (Test)

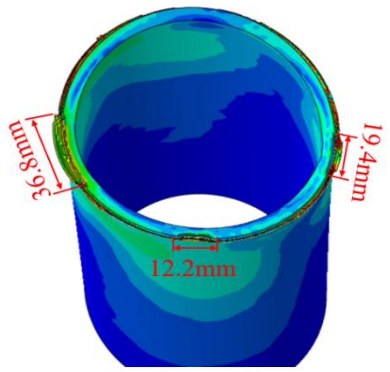

(b) Fracture point (FEA)

Fig. 18 Weld fracture comparison of GX-2

(a) Fractured in the front side (Test)

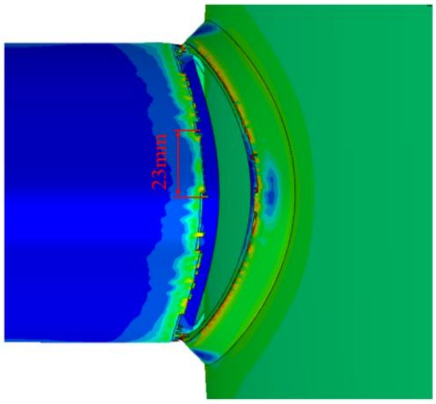

(b) Fractured in the front side (FEA)

(c) Specimen in the behind side (Test)

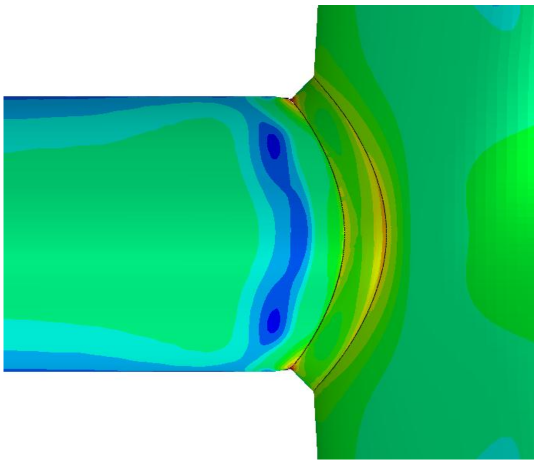

(d) Specimen in the behind side (FEA)

Fig. 19 Weld fracture comparison of GX-3

As shown in Figs. 18 and 19, the FEA results of specimens GX-2 and GX-3 are basically consistent with the fracture phenomenon of the test results. The stress concentration at the joint's saddle point is relatively severe, causing weld cracking at the CHS-X joint's saddle point. For specimen GX-2, the dimensions and positions of the chord deformation and brace fracture points simulated by FEA are basically the same as those of the test. The FEA and test of GX-3 indicate that the front side of the joint has experienced a fracture, while the rear of the joint does not show obvious failure characteristics except for large stress concentration. This proved that the simplified weld defects of the specimens GX-2 and GX-3 and the constraint imposed between the weld and the brace after the simplified weld defects were reasonable.

4.4. Load-displacement curves

The load-displacement curves for the FEA and test, as depicted in Figs.20, 21, and 22, exhibit similar trends and consistency. As shown in Table 4, the displacement error of the joints simulated by the VGM model without weld defects of GX-1 and with weld defects of GX-2 and GX-3 welds is 19.5%, 19.49%, and 19.97%, respectively, the load error is 19.48%, 20.45%, and 21% respectively, and the error is within 21%. The displacement error of the joints simulated by the SWDM model without weld defects of GX-1 and with weld defects of GX-2 and GX-3 welds is 5.77%, 8.67%, and 7.62%, respectively, and the load error is 11.92%, 16.93%, and 16.12% respectively, with the error within 17%. It can be seen that both the SWDM model and the VGM model can be used to predict the ultimate bearing capacity of CHS-X joints with weld defects. This is consistent with the conclusion that the micromechanical fracture models VGM and Stress Modified Critical Strain (SMCS) discussed in the literature [28] are applicable to the fracture prediction of beam-column joints with initial defects. SWDM model performs better than the VGM model in CHS-X joint fracture prediction.

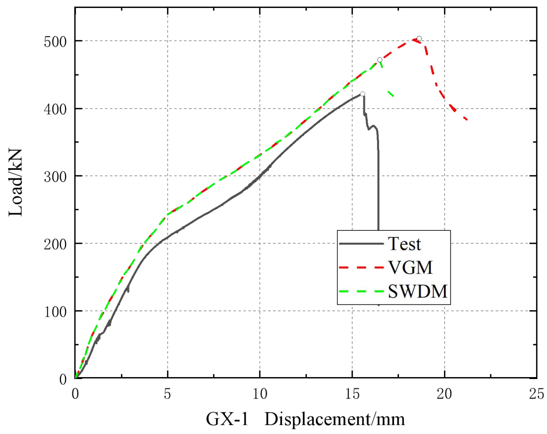

Fig. 20 FEA and test load-displacement curves for GX-1

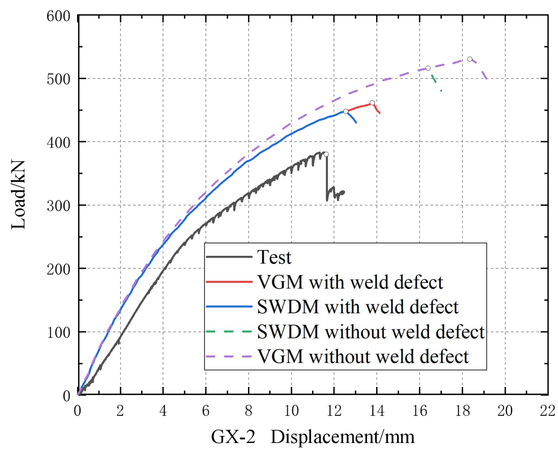

Fig. 21 FEA and test load-displacement curves for GX-2

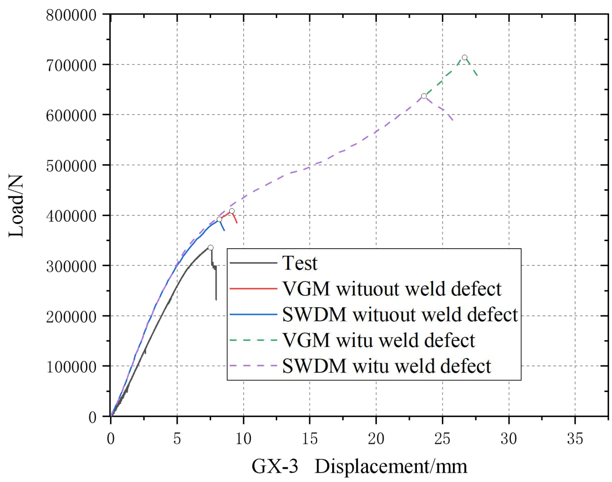

Fig. 22 FEA and test load-displacement curves for GX-3

Both SWDM and VGM can accurately predict the weld fracture of the CHS-X joint; However, considering the influence of the Lord's angle parameter, SWDM can accurately simulate the damage degree of the joint under different stress states, and its accuracy is higher than that of VGM, with good applicability [46]. At the same time, the equivalent area method and the equivalent width method are used to simplify the weld defect, and the influence of the weld defect shape on the joint is ignored. Only the influence of the weld defect position on the joint is considered, and the influence of the stress concentration and the local weld defect shear force is not considered. Therefore, the calculation results of the SWDM model and the VGM model are different, and the performance of the SWDM model is better than the VGM model.

This article employs the equivalent area method and the equivalent width method to simplify the analysis of weld penetration depth. The influence of weld defect shapes on the joint is primarily attributed to specific stress concentrations caused by irregular shapes, which have not been fully considered. Instead, the focus is on the impact of incomplete fusion locations and areas within the weld seam on the joint. Additionally, securing the end of the chord during load testing can be challenging. As the load increases, the fixed reaction frame tends to slide, introducing a certain degree of error into the test. Finite element modelling and simulation operate under ideal conditions, which contribute to discrepancies when compared to experimental results. Specifically, the finite element simulation results indicate that the VGM model has an error of nearly 20%, whereas the SWDM model exhibits an error of approximately 17%.

By comparing joint test and FEA results, VGM and SWDM models are used to predict the crack propagation process of joints and the ultimate bearing capacity of joints, which are in good agreement with the test results, proving the rationality of simplification of weld defects. FEA Comparison of Specimens with and without weld defects, the ultimate bearing capacity of GX-2 drops by 15%, the fracture displacement drops by 34.3%, the ultimate bearing capacity of GX-3 drops by 76.2%, and the fracture displacement drops by 189.7%. It can be seen that the existence of weld defects greatly influences the ultimate bearing capacity and fracture displacement of the CHS-X joints. Studying the impact of weld imperfections on the load-bearing capability of CHS-X joints can offer valuable insights for the safety assessment of CHS-X joints with weld defects.

Table 4
Load-displacement comparison between test and FEA results

Specimen	FEA (VGM)		Test		Displacement error	Load error
	Ultimate load (*kN*)	Δ_u/mm	Ultimate load (*kN*)	Δ_u/mm		
GX-1	503.67	18.63	421.55	15.59	19.5%	19.48%
GX-2 with weld defects	530.79	18.52	-	-	-	-
GX-2 without weld defects	461.37	13.79	383.04	11.54	19.49%	20.45%
GX-3 with weld defects	719.83	26.45	-	-	-	-
GX-3 without weld defects	408.39	9.13	337.42	7.61	19.97%	21%

Specimen	FEA (SWDM)		Test		Displacement error	Load error
	Ultimate load (*kN*)	Δ_u/mm	Ultimate load (*kN*)	Δ_u/mm		
GX-1	471.81	16.49	421.55	15.59	5.77%	11.92%
GX-2 with weld defects	515.95	16.30	-	-	-	-
GX-2 without weld defects	447.89	12.54	383.04	11.54	8.67%	16.93%
GX-3 with weld defects	641.05	23.45	-	-	-	-
GX-3 without weld defects	391.82	8.19	337.42	7.61	7.62%	16.12%

5. Conclusion

In order to study the fracture behavior of the CHS-X joints with initial defects, an axial test is designed for one weld penetration test piece and two test pieces without weld penetration. The Void Growth Model (VGM) and Stress Weighted Damage Model (SWDM) are programmed into the program of ABAQUS software VUSDFLD by Frotran language. The FEA of the CHS-X joints with initial defects was carried out, and the applicability of the two models in the fracture prediction of CHS-X joints with initial defects is discussed by comparing them with the test results. The following main conclusions are drawn from this study:

(1) The FEA of the GX-1 specimen with no weld defects is in good agreement with the test results, which indicates that the VGM and SWDM models can be used to predict the fracture of the joints effectively.

(2) Based on the irregularity of weld defects, finite element modelling is difficult. According to the actual welding condition of the weld, the equivalent width method and the equivalent area method are used to simplify the weld defects and establish the corresponding finite element model. VGM and SWDM models are used to predict the crack propagation process and the ultimate bearing capacity of the joints, which are in agreement with the test results, and the fracture phenomenon is basically the same. It is proved that the two models can effectively predict the fracture of the joints weld with defects and the rationality of simplifying the weld defects.

(3) By comparing the fracture displacement and ultimate load of the test and FEA, it can be found that the error of the VGM model is within 21%, and the error of the SWDM model is within 17%. The fracture prediction results of weld fracture of the CHS-X joints by the SWDM model are closer to the test results than those of the VGM model. This shows that the SWDM model can be well applied to the fracture prediction and fracture path simulation of the CHS-X joints defects weld.

Acknowledgements

The research presented in this paper was supported by the Natural Science Foundation of China (NSFC) through Grant No.51368009 and was also supported by the Natural Science Foundation of Guizhou province (CN) through Grant No. (2018) 1036.

Reference

[1] F.F. Liao, K.K. Li, W. Wang, Y.Y. Chen, G. Li, Experimental study and finite element analysis on fracture performance of ER55-G welds. *Journal of Constructional Steel Research*, 2020, 172: 106129.
[2] X. Chang, L. Fu, H.B. Zhao, Y. B. Zhang, Behaviors of axially loaded circular concrete-filled steel tube (CFT) stub columns with notch in steel tubes. *Thin-Walled Structures*, 2013, 73: 273-280.
[3] F.X. Ding, L. Fu, Z.W. Yu, Behaviors of axially loaded square concrete－filled steel tube (CFST) stub columns with notch in steel tube. *Thin － Walled Structures*, 2017, 115: 196-204.
[4] J.F. Geng, H.S. Cai, X. P. Liang, H. Wang, Y. J. Wang, Z.H. Wang, Welding Defect Analysis in Thin-Walled Steel Tube under Bending Moment. *Applied Mechanics and Materials*, 2011, 94: 1711-1714.
[5] M. Yan, Z. Guo, C. Li, Y. Liu, X. Wang, Effect of welding defects on mechanical properties of welded joints subjected to temperature. *Steel and Composite Structures, An International Journal*, 2021, 40(2): 193-202.
[6] S. Tang, X. Gao, K. Tian, Q. Zhang, X. Zhang, J. Peng, J Guo, Non-destructive evaluation of weld defect with coating using electromagnetic induction thermography, *Nondestructive Testing and Evaluation*, 2024, 39(2): 347-365.
[7] D. Shiraishi, R. Kato, H. Endoh, T. Hoshimiya, Destructive inspection of weld defect and its nondestructive evaluation by photoacoustic microscopy. *Japanese Journal of Applied Physics*, 2010, 49(7S): 07HB13.
[8] A. A. Griffith, VI. The phenomena of rupture and flow in solids. *Philosophical transactions of the royal society of london. Series A, containing papers of a mathematical or physical character*, 1921, 221(582-593): 163-198.
[9] G. R. Irwin, Analysis of stresses and strains near the end of a crack traversing a plate. (1957):361-364
[10] J.R. Rice, A path independent integral and the approximate analysis of strain concentration by notches and cracks. *Journal of Applied Mechanics*, 1967.
[11] J. R. Rice, D. M. Tracey, On the ductile enlargement of voids in triaxial stress fields∗. *Journal of the Mechanics and Physics of Solids*, 1969, 17(3): 201-217.
[12] Z.H. Huang, M. Ashraf, T. Zheng, Y. Yang, E.H. Bao, H. Han, Analysis of ultimate fracture bearing capacity of CHS XK-joints welds, *Sustainable Structures*. 2023, 3(2): 000031.
[13] A.M. Kanvinde, G.G. Deierlein, Finite-element simulation of ductile fracture in reduced section pull-plates using micromechanics-based fracture models. *Journal of Structural Engineering*, 2007, 133(5): 656-664.
[14] F.F. Liao, W. Wang, Y.Y. Chen, Parameter calibrations and application of micromechanical fracture models of structural steels, *Structural engineering and mechanics,* 2012, 42(2): 153-174.
[15] X. Qu, C. Qin, G. Sun, Y. Xie, Research on fracture of steel structure welded joint based on micro-mechanism. *Structures,* 2022, 43: 434-448.
[16] Y. Wang, H. Zhou, Y. Shi, J. Xiong, Fracture prediction of welded steel connections using traditional fracture mechanics and calibrated micromechanics based models. *International Journal of Steel Structures*, 2011, 11: 351-366.
[17] Y. Yin, X. Che, Z. Li, J. Li, & Q. Han, Ductile fracture analysis of welded hollow spherical joints subjecting axial forces with micromechanical fracture models. *International Journal of Steel Structures*, 2019, 19: 2010-2023.
[18] F.F. Liao, Y. Liu, W. Wang, Z. Lu, X. Li, Fracture performance study on Q460D steel and ER55-G welds after high temperature. *Journal of Constructional Steel Research*, 2023, 206: 107888.
[19] Y. Yin, X. Liu, Q. Han, Z. Liu, Simulation of ductile fracture of structural steels with void growth model and a continuum damage criterion based on it. *Theoretical and Applied Fracture Mechanics*, 2018, 98: 134-148.
[20] A. M. Kanvinde, G. G. Deierlein, Cyclic void growth model to assess ductile fracture initiation in structural steels due to ultra low cycle fatigue. *Journal of engineering mechanics*, 2007, 133(6): 701-712.
[21] J.Y. Han, J. Li, Y. Yang, Q. Xiang, Z. Huang, Numerical simulation of the crack propagation effect on the hysteretic behavior of CHS-X joints. *Engineering Failure Analysis*, 2024: 108549.
[22] C. M. Smith, A Stress-weighted Damage Model for Ductile Fracture Initiation in Structural Steel Under Cyclic Loading and Generalized Stress States, Stanford University, 2013.
[23] X. He, Q. Luo, Y. Yang, Z. Huang, Calibration of micromechanical fracture model parameters for Q355B steel and ER50–6 welds. *Journal of Constructional Steel Research*, 2024, 215: 108563.
[24] T. Lin, W. Huang, S.W. Liu, & R. Bai, AN INVESTIGATION ON THE EFFECT OF RANDOM PITTING CORROSION ON THE STRENGTH OF THE SUBSEA PIPELINE USING MONTE CARLO METHOD. *Advanced Steel Construction*, 2024, 20(1): 93–104.
[25] Q. Si, Y. Ding, L. Zong, & H.T. Zhao, MECHANICAL BEHAVIOUR OF CORRODED STRUCTURAL STEEL SUBJECTED TO MONOTONIC TENSION. *Advanced Steel Construction*, 2022, 18(3): 707-714.
[26] Z.Y. Jie, W.J. Wang, P. Zhuge, Y.D. Li, & X. Wei, FATIGUE PROPERTIES OF INCLINED CRUCIFORM WELDED JOINTS WITH ARTIFICIAL PITS. *Advanced Steel Construction,* 2021, 17(1): 20-27.
[27] Z.W. Zhang, H.J. Wang, H.L. Qian, X.F. Jin, Q. F, & F. Fan, RESIDUAL LIFE PREDICTION AND DESIGN CORRECTION METHOD OF CORRODED CIRCULAR STEEL TUBES BASED ON TIME-VARYING RELIABILITY. *Advanced Steel Construction,* 2024,20(1): 12-20.
[28] L.F. Xiao, J.X. Peng, J.R. Zhang, & C.S. Cai, MECHANICAL PROPERTIES OF CORRODED HIGH PERFORMANCE STEEL SPECIMENS BASED ON 3D SCANNING. *Advanced Steel Construction,* 2019, 15(2): 129-136.
[29] M. Arandelović, S. Sedmak, R. Jovičić, S. Perković, Z. Burzić, D. Radu, Z. Radaković, Numerical and experimental investigations of fracture behaviour of welded joints with multiple defects. *Materials*, 2021, 14(17): 4832.
[30] L. Zhu, N. Li, B. Jia, Y. Zhang, Fracture response of X80 pipe girth welds under combined internal pressure and bending moment. *Materials*, 2023, 16(9): 3588.
[31] L. Mazurkiewicz, M. Tomaszewski, J. Malachowski, K. Sybilski, M. Chebakov, M. Witek, ... & R. Dmitrienko, Experimental and numerical study of steel pipe with part-wall defect reinforced with fibre glass sleeve. *International Journal of Pressure Vessels and Piping*, 2017, 149: 108-119.
[32] H.S. Lai, S.H. Kil, K.B. Yoon, Effects of defect size on failure of butt fusion welded MDPE pipe under tension. *Journal of Mechanical Science and Technology*, 2015, 29: 1973-1980.
[33] Y.B. Wang, Z.W. Guo, X.Q. Bai, C.Q. Yuan, Effect of weld defects on the mechanical properties of stainless-steel weldments on large cruise ship. *Ocean Engineering,* 2021, 235: 109385.
[34] M. Yan, Z. Guo, C. Li, Y. Liu, X. Wang, Effect of welding defects on mechanical properties of welded joints subjected to temperature. *Steel and Composite Structures, An International Journal,* 2021, 40(2): 193-202.
[35] M. Arandjelovic, B. Djordjevic, S. Sedmak, D. Radu, A. Petrovic, S. Dikic, A. Sedmak, Failure analysis of welded joint with multiple defects by extended Finite Element Method and Engineering Critical Analysis. *Engineering Failure Analysis,* 2024, 160: 108176.
[36] F.F. Liao, K. Zhang, W. Wang, Y. Chen, S. Tang, X. Xue, & C. Li, Fracture analysis of high-strength steel beam-column connections with initial defects. *Journal of Constructional Steel Research*, 2022, 194: 107301.
[37] J.H. Xing, D. Dilixiati, N. Yang, Q.S. Yang, Fracture properties of corroded steel under monotonic tension load. *Construction and Building Materials,* 2024, 437: 136918.
[38] GB / T 228.1-2021, Tensile testing of metallic materials--Part 1: Room temperature test method.
[39] EN ISO 6892-1: 2019, Metallic Materials - Tensile Testing - Part 1: Room Temperature Test Method.

[40] ABAQUS, Analysis User's Manual Version 6.14-4, Dassault Syst`emes Simulia Corp, Providence, RI, USA, 2010.

[41] B. Chen, Safety analysis of in-service pressure pipelines with incomplete penetration defects based on maximum load. Zhejiang University, 2010. (in Chinese)

[42] H.Y. Xiong, Research on the Ultimate Load Carrying Capacity of Steel Pipes with Ring Weld Defects. Southwest University of Science and Technology, 2023. (in Chinese)

[43] Q. Zhao, K. Tang, G.M. Huang, & Z.Z Lin, Effect of initial defect of butt weld on fatigue life. *Journal of Hefei University of Technology (Natural Science),* 2023, 46(04):473-480. (in Chinese)

[44] K. Yang, H. Feng, P. Wang, H.Y. Cheng, Q. Chi, Evaluation of Girth Weld Tensile Capaity of High Grade Pipeline Based on Full Size Test. *Petroleum Tubular Goods & Instruments,* 2022, 8(06):44-49. (in Chinese)

[45] Z.L. Liu, Ductility fracture test and finite element analysis of X-shaped circular steel tube intersecting nodes under static load. Guizhou University, 2023. (in Chinese)

[46] H. Han, T. Zheng, X.D. Wang, Z. H. Huang, Fracture prediction and bearing capacity analysis of weld of tubular circular hollow section X-joints. *Building Structures,* 2022, 52(13):99-105. (in Chinese)